Chapter 8. Ocean Currents and Current Gradients

David R. Lyzenga
Department of Naval Architecture and Marine Engineering University of Michigan Ann Arbor, MI, USA

George O. Marmorino
Remote Sensing Division, Naval Research Laboratory, Washington, D.C.USA

Johnny A. Johannessen
Nansen Environmental and Remote Sensing Center (NERSC), Bergen, Norway

8.1 Introduction

Ocean currents influence global and local climates and impact marine and terrestrial life through the redistribution of heat, nutrients, and pollutants. Many of these processes are influenced by the strong current gradients that exist near the boundaries of major current systems and in regions of outflow from rivers and estuaries. Frontal instabilities cause these boundaries to frequently evolve into meanders which may ultimately break off to form eddies. Deep-water current gradients are typically characterized by a mixture of (1) cyclonic or anticyclonic shear in geostrophic balance, and (2) ageostrophic flow across the frontal boundary. Although the ageostrophic component is usually much weaker than the geostrophic component, it can have a significant impact on the three-dimensional circulation patterns in the frontal region, and thus on physical and biochemical conditions in the mixed layer, via the downwelling or upwelling circulation associated with the surface current convergence or divergence in the frontal vicinity.

Ocean current boundaries are often accompanied by changes in surface roughness that can be detected by synthetic aperture radar (SAR) and other imaging radar systems. These surface roughness changes are due to three main mechanisms. The first mechanism involves the accumulation of naturally occurring (biogenic) surfactant materials in regions of converging surface currents [*Ochadlick et al.*, 1992; *Gower*, 1994]. These materials attenuate short (cm to dm scale) surface waves and hence reduce the radar backscatter. The resulting dark bands in imagery not only indicate regions of convergence, but also act as passive tracers, as discussed in Section 8.2. The second mechanism involves the interaction of surface waves directly with surface current gradients [*Lyzenga*, 1991; 1998]. These interactions can cause either an increase or decrease in the surface roughness depending on the type of current gradient (convergence, divergence, or shear) and the wave propagation direction. Therefore, these interactions may be manifested by either bright or dark bands in the imagery. In some cases, changes in the wavelength and/or direction of longer waves can be observed directly and used to infer the underlying currents [*Sheres*, 1982; *Beal et al*., 1986; *Barnett et al*., 1989]. The final mechanism is due to atmospheric stability effects associated with the surface temperature gradients that frequently accompany current systems [*Brown*, 1990; *Wu*, 1991; *Beal et al*, 1997]. Convective instabilities occur in regions where the air temperature is lower than the water temperature, as the air in contact with the water becomes heated. These instabilities cause an increase in near-surface wind stress which, in turn, increases the surface roughness and the radar backscatter. Examples of each of these mechanisms are presented in the following sections.

Current boundaries can frequently be observed in radar images, even in the presence of clouds that may obscure visible or infrared images. However, these features depend on environmental conditions, and are ambiguous in the sense that they may be similar to features caused by other phenomena. For example, the effects of surface slicks and of wave-current interactions decrease with increasing wind speed, while atmospheric stability effects depend on the temperature of the air relative to that of the water. Therefore, interpretation of SAR images requires a knowledge of the general environmental conditions and may be aided by comparisons with imagery from other types of sensors. For example, thermal fronts can be observed by infrared radiometers under cloud-free conditions, and the use of such imagery is frequently helpful in interpreting SAR images [*Fu and Holt*, 1982; 1983]. Surface slicks may also be expressed via sunglitter in visible images, as recently demonstrated by Munk *et al.* [2000] in a comprehensive study of 10-25 km spirals on the sea using space photography and imaging radar.

This chapter provides examples of current-related image features and discusses the relationships between these features and the underlying current fields. Examples include the Norwegian Coastal Current, the Gulf Stream, and coastal fronts associated with the Chesapeake Bay outflow, arranged roughly from larger to smaller spatial scales.

8.2 Norwegian Coastal Current

A good example of SAR-observed surface features associated with mesoscale circulation patterns is presented in Figure 8.1. This figure shows a thermal infrared (IR) image (left) from the National Oceanic and Atmospheric Administration's (NOAA) Advanced Very High Resolution Radiometer (AVHRR) and an ERS-1 SAR image (right) acquired about seven hours later on 3 October 1992 off the west coast of Norway. The fairly weak temperature contrast shown in the AVHRR image is typical of the late fall time period. The maximum temperature gradient is about 0.6°C km^{-1}. Previous observations across such temperature fronts have established corresponding salinity and density fronts, which combine to maintain a baroclinic current boundary. The structure of the sea surface temperature field suggests mesoscale variability of 10 km to 50 km scale, characteristic of the unstable Norwegian Coastal Current [*Johannessen et al*., 1989].

The ERS-1 SAR image contains frontal features at a scale, configuration, and orientation in agreement with those seen in the IR image. The SAR image shows both bright and dark radar cross-section modulations of various widths across the boundaries. This comparison clearly verifies that a SAR can image current boundaries, including meanders. Based upon the surface weather analysis, winds were northerly at 5 m s^{-1} and air temperatures ranged from 12° to 14°C along the coast where the SAR image was acquired. A moored buoy deployed about 20 km offshore reported a northward near-surface current of 0.30 m s^{-1}, a water temperature of about 13.5°C, and a significant wave height of 1 m at the satellite overpass time [*Johannessen et al*., 1996]. The agreement between the locations and shapes of the meandering frontal features in the two images suggests that the same basic oceanic processes are being imaged by both sensors.

The air-sea temperature difference indicates near neutral atmospheric stability. An analysis was conducted [*Johannessen et al.*, 1996] to determine whether the SAR image patterns could be caused by atmospheric stability effects. This analysis indicated that the observed backscatter variations would require an air-sea temperature difference of –6°C to –12°C. Since a temperature difference of this magnitude was not present, we conclude that the SAR image expressions for this case are primarily due to wave-current interactions involving short gravity waves along the current fronts. This conclusion is strengthened by an analysis of the sign of the

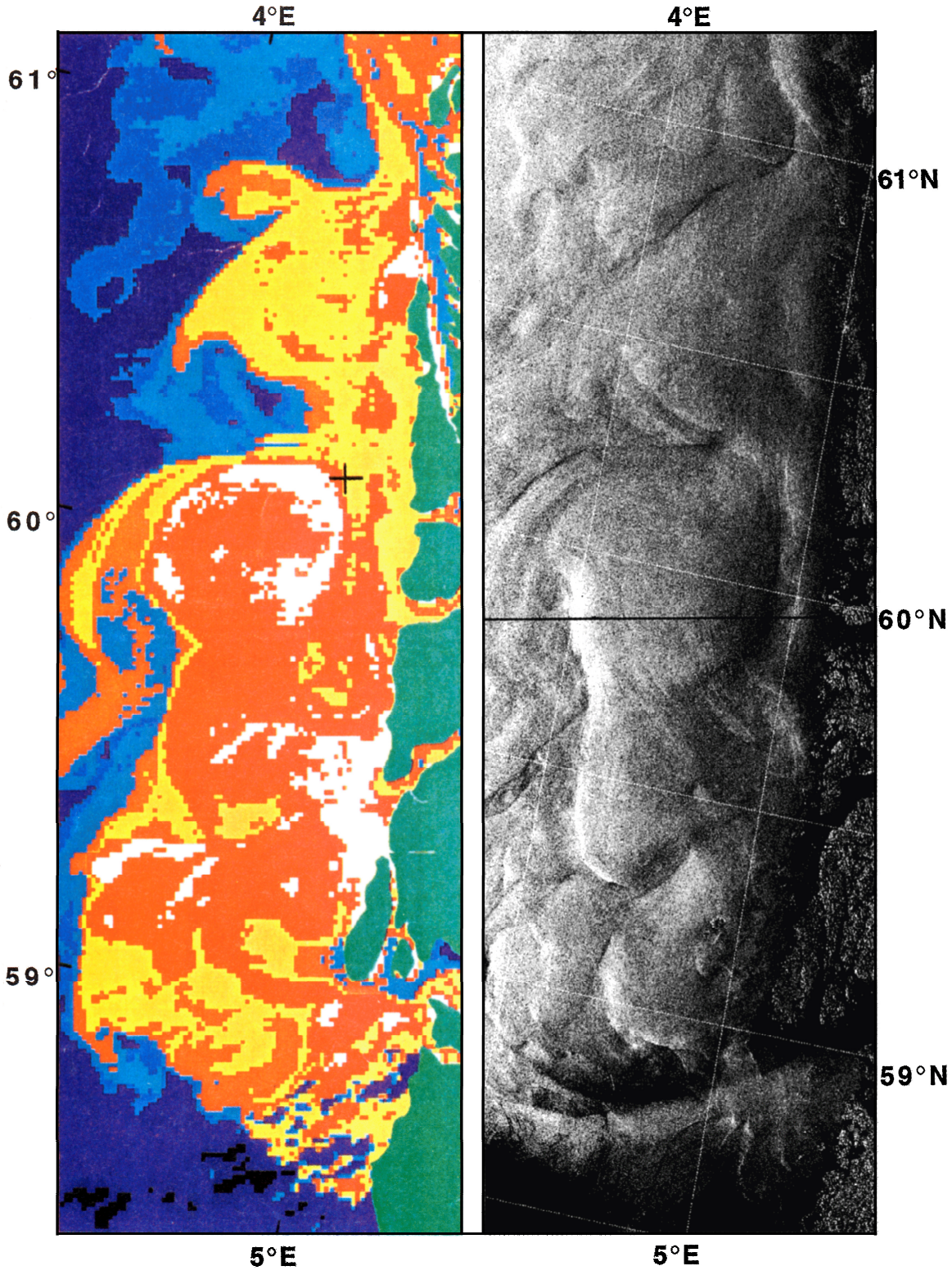

Figure 8.1. Mesoscale current features in the Norwegian Coastal Current as imaged by the NOAA AVHRR (thermal infrared) (left) at 1420 UTC and by the ERS-1 (C-band, VV) SAR (right) at 2135 UTC on 3 October 1992. Surface temperatures indicated by AVHRR image range from 12 °C (dark blue) to 14 °C (white). Each image covers an area of 100 km x 300 km. [Aftrer *Johannessen et al.*, 1996]

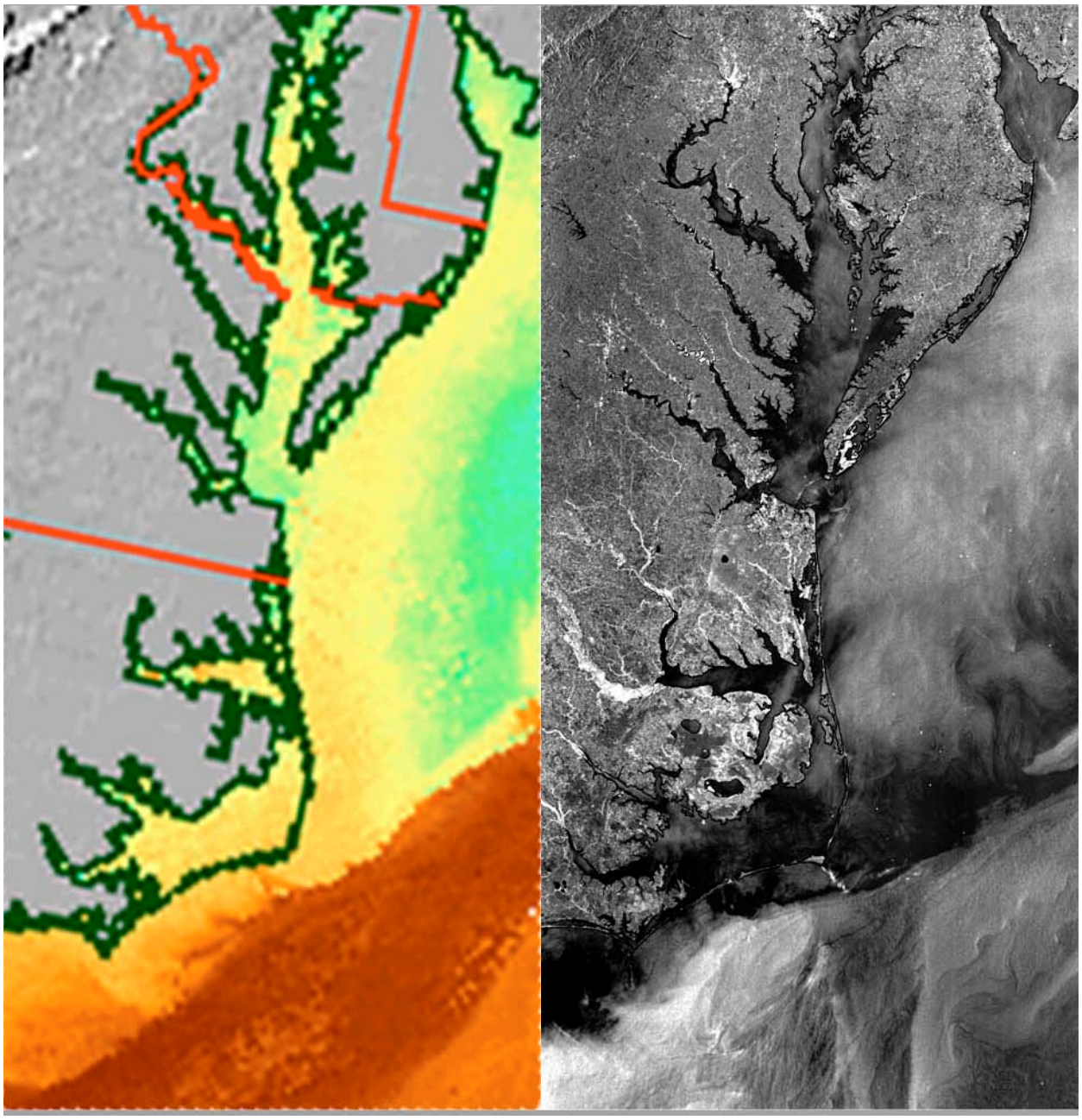

Figure 8.2. The Gulf Stream off North Carolina imaged via AVHRR (thermal infrared) (left panel - 1300 UTC) and RADARSAT-1 (C-band, HH) (right panel - 2300 UTC) on 16 October 1996 under low winds (between 2 and 3 m s^{-1}). Surface temperatures in AVHRR image range from 15°C (light green) to 30°C (red). The imaged areas are each approximately 300 km wide. [After *F. Monaldo, R. Beal, and D. Thompson, http://fermi.jhuapl.edu/sar/compendium*, 2002]. RADARSAT-1 image ©CSA 1996

radar cross section perturbations (i.e., the presence of bright or dark lines) for the features in Figure 8.1, and for similar features observed in both aircraft and ERS satellite imagery over this area [*Lyzenga and Wackerman*, 1997]. Wave-current interaction theory predicts that for shear-dominated current gradients; the sign of the perturbation varies with look direction in a manner consistent with the observed features in these images.

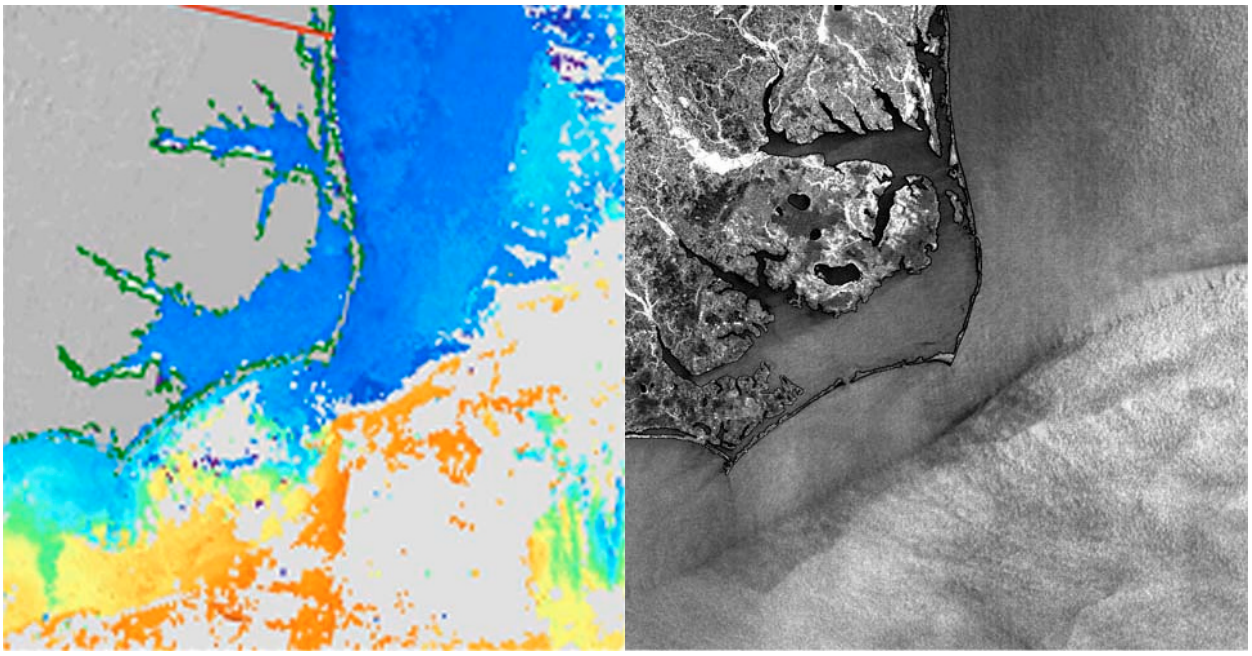

Figure 8.3. The Gulf Stream off North Carolina imaged via AVHRR (thermal infrared) (left panel - 1300 UTC) and RADARSAT-1 (C-band, HH) (right panel - 2300 UTC) on 13 February 1997 under high winds (14 to 16 m s^{-1}). Surface temperatures in AVHRR image range from 8 °C (blue) to 22 °C (orange). The imaged areas are each approximately 300 km wide. [After *F. Monaldo, R. Beal, and D. Thompson, http://fermi.jhuapl.edu/sar/compendium,* 2002]. RADARSAT-1 image ©CSA 1997

8.3 Western Gulf Stream

Features associated with the Gulf Stream boundary were observed in SEASAT images [*Hayes*, 1981; *Fu and Holt*, 1982; 1983] and later in ERS-1 images [*Beal et al*., 1997]. Several examples illustrating the appearance of the Gulf Stream boundary in RADARSAT-1 images under different wind conditions are shown in Figures 8.2, 8.3 and 8.4 (additional ERS examples can be found at http://fermi.jhuapl.edu/sar).

Figure 8.2 shows the northern edge of the Gulf Stream near Cape Hatteras, North Carolina as imaged by the AVHRR IR sensor (left panel) and the RADARSAT-1 SAR (right panel) on 16 October 1996. The wind speed at the time of the RADARSAT-1 overpass was between 2 m s^{-1} and 3 m s^{-1} from the northwest, as measured at NOAA buoy DSLN7 (just off Cape Hatteras). The warmer Gulf Stream water appears brighter in the SAR image, probably because of the atmospheric stability effect discussed in the previous section, since the air flowing from the northwest onto the warmer Gulf Stream would be expected to produce unstable conditions. Wave-current interactions may cause the subtle modulations within the Gulf Stream.

Figure 8.3 shows a similar comparison of AVHRR and RADARSAT-1 images under higher winds (between 14 m s^{-1} and 16 m s^{-1}) on 13 February 1997. In this case, the AVHRR image is partially obscured by clouds (white), but a general correspondence still exists between the Gulf Stream boundary locations as indicated by the IR and SAR images. The boundary in the SAR image in this case is demarcated by a narrow dark line that may be caused by the accumulation of surfactants. Alternatively, the dark region may indicate a transition from near neutral atmospheric stability over the Gulf Stream to highly stable conditions to the west, since the wind was from the east in this case.

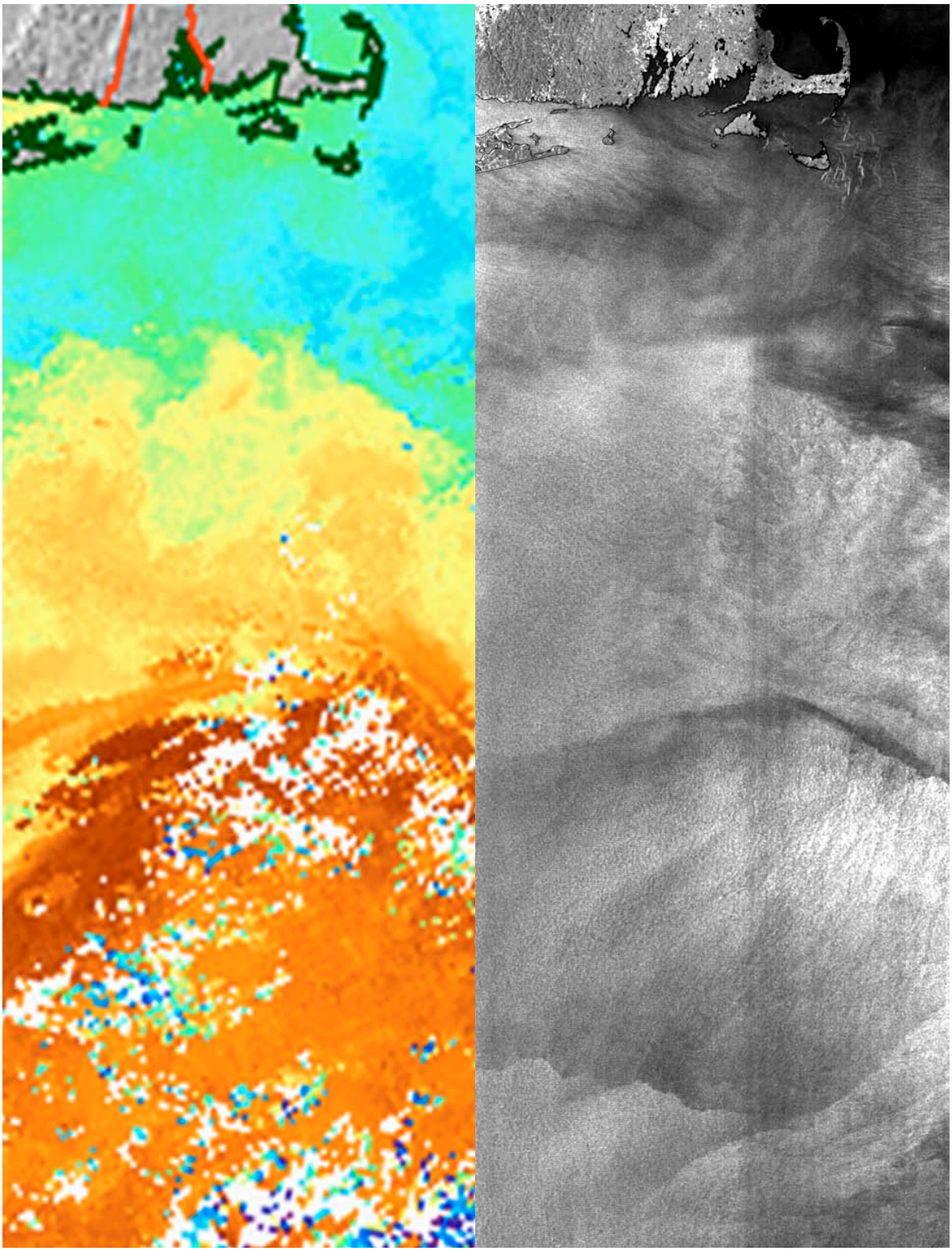

Figure 8.4. The Gulf Stream off the U.S East Coast imaged AVHRR image (left panel - 1300 UTC) and RADARSAT-1 (C-band, HH) (right panel - 2300 UTC) on 10 October 1996 under moderate winds (6 to 8 m s^{-1}). Surface temperatures in AVHRR image range from 10°C (light blue) to 30°C (red). The imaged areas are each approximately 300 km wide. [After *F. Monaldo, R. Beal, and D. Thompson, http://fermi.jhuapl.edu/sar/compendium, 2002*]. RADARSAT-1 image ©CSA 1996

Figure 8.4 shows a strip of RADARSAT-1 imagery, along with the corresponding AVHRR image, acquired on 10 October 1996 about 600 km east of the previous images shown in Figures 8.2 and 8.3. The wind speed was between 6 m s^{-1} and 8 m s^{-1}, as measured at NOAA buoy 41001 (34° 41′ N, 72° 38′ W). The main Gulf Stream boundary, just below the center of the image, appears as a dark line in the SAR image. A secondary thermal boundary farther to the north also shows up clearly as a difference in backscatter. However, several distinct features near the bottom of the SAR image do not have any clear counterparts in the IR imagery. Some of the differences may be attributed to the time delay between the images. Other differences may be caused by processes such as small-scale mixing, eddies, and the formation of atmospheric fronts near the thermal boundaries. The discontinuity in sea surface temperature along the edge of the Gulf Stream affects the atmospheric boundary layer wind fields on a variety of scales. In particular, the mesoscale solenoidal flow can lead to frontogenesis, so that a wind front can often be found nearly parallel to the ocean front but possibly offset by synoptic winds or by frontal propagation. Further examples of atmospheric fronts along the Gulf Stream boundary are shown in the aircraft SAR images discussed in the following paragraphs.

Figures 8.5 (a) and (b) show two smaller-scale airborne SAR images acquired about 20 minutes apart near the northwestern boundary of the Gulf Stream east of Cape Hatteras, at approximately 35.3^{o}N and 75.0^{o}W. A variety of surface features appear in these images, as identified in (c), including a large number of narrow slicks that were advected by the Gulf Stream currents during the 20 minute interval between frames (a) and (b). The displacements of several of the slicks during this interval, indicated by arrows in (b), were measured by computing the local cross-correlation function for the two images. The currents that are inferred from these displacements agree with shipboard ADCP measurements along the tracks shown by the dotted lines in (b) with an root mean square (rms) difference of approximately 4 cm s^{-1} for the easterly component and 13 cm s^{-1} for the northerly component of the current (the mean current was 67 cm s^{-1} to the east and 102 cm s^{-1} toward the north). Part of the difference between these measurements may be caused by wind drift, since the slicks are confined to a very thin surface layer.

The example in Figure 8.5 shows that quantitative surface currents can be obtained from pairs of suitably acquired SAR images, provided that surface features such as those shown in Figure 8.5 exist within the images. Of course, such features do not always occur, and it is rarely possible to obtain pairs of images with a suitable time spacing from existing spaceborne SAR systems. Surface slicks occur frequently near current boundaries and it may be possible to infer something about the currents from the orientation of the slicks observed within a single image. However, as shown in Figure 8.5 and as discussed in *Lyzenga and Marmorino* [1998], the orientations of the slicks are related more closely to the current gradients than to the current direction. The orientation of the slicks in Figure 8.5 was well reproduced by a simple surface deformation model using the measured current gradients.

Also shown in Figure 8.5 is a wind front that corresponds roughly with the northern edge of the Gulf Stream. The wind speed or wind stress is above the threshold for wave generation on the southeast side of this front and below the threshold on the northwest side, leading to the large difference in backscatter that is visible in the images. Closer inspection shows that the position of the wind front has translated about 2 km between the images, corresponding to a speed of about 1.7 m s^{-1}. Such wind fronts can be confused with current or temperature fronts, although to the extent that wind fronts are correlated (as in this case), they may be used as crude indicators of current boundaries. Time lapse images such as those shown in Figure 8.5 can be used to

(a)

(b)

(c)

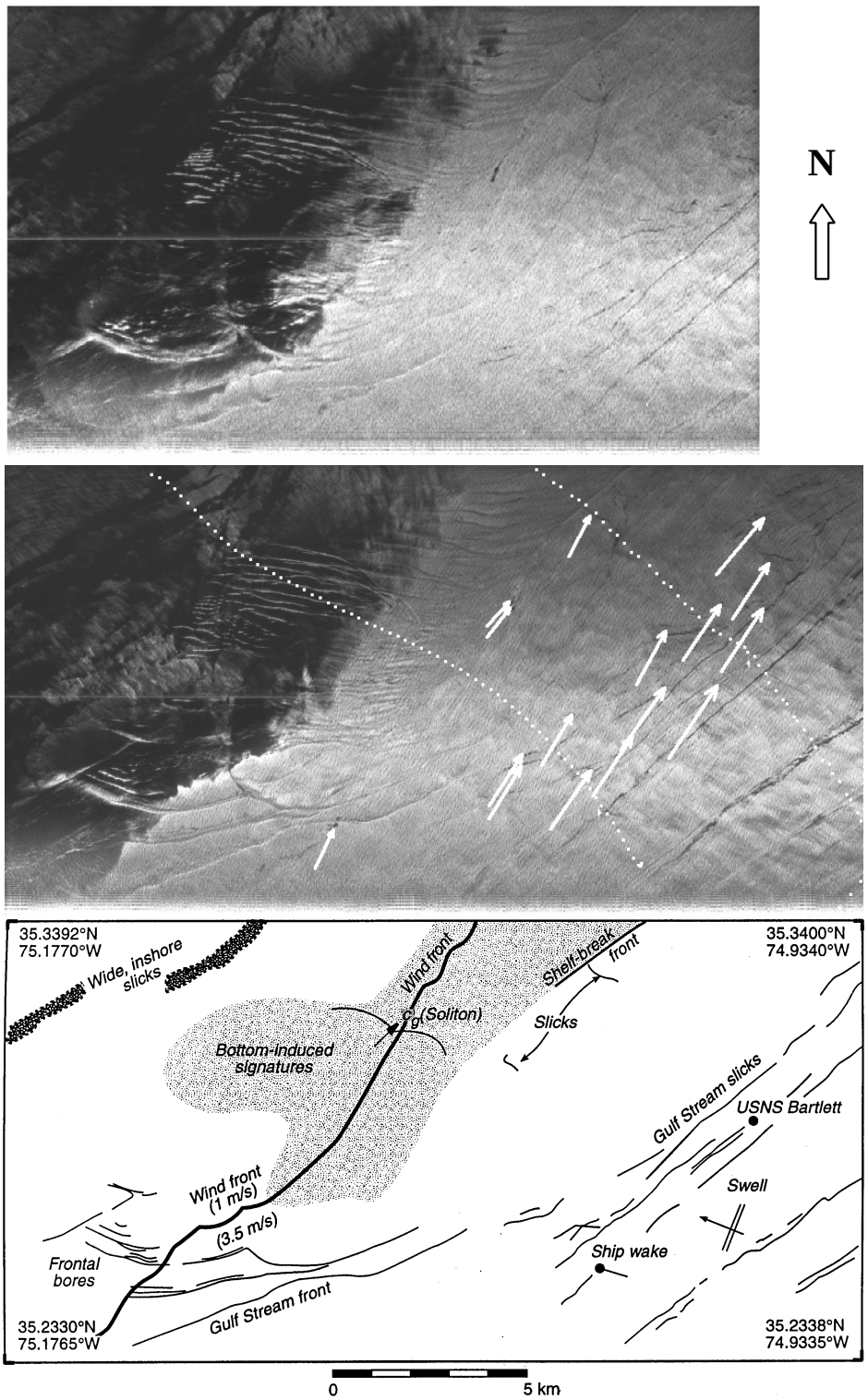

Figure 8.5. Airborne SAR images acquired by the ERIM/NAWC SAR (L-band, VV) system off Cape Hatteras, North Carolina. Image (a) was acquired at 1630 UTC and image (b) was acquired at 1650 UTC on 16 September 1991. Superimposed on (b) are the surface current vectors obtained by tracking surface slick features that appear in both images (dotted curves indicate ship tracks). Panel (c) identifies several other features appearing in the images. After *Lyzenga and Marmorino*, 1998]. The ERIM/NAWC SAR system was built by the Environmental Research Institute of Michigan and operated by the Naval Air Warfare Center.

distinguish these types of wind fronts, although image pairs are not presently available from spacecraft platforms, as noted previously.

8.4 Estuarine outflows and channel convergence fronts

Figure 8.6 is an ERS-1 SAR image showing the mouth of the Chesapeake Bay, which is the largest estuary in the United States. The data were acquired in the spring when the total river discharge rate into the bay is relatively high (about 3000 $m^3 s^{-1}$) but images obtained at other times of the year show similar features. As relatively fresh water is discharged on successive ebb tidal cycles, a shallow salinity front develops and moves outward with the current into the denser continental shelf water. The front is narrow ($\leq$10 m wide) and has strong surface current convergence [*Marmorino and Trump*, 2000]. In Figure 8.6, the seaward edge of the outflowing plume is delineated by a high-backscatter (relatively bright) frontal signature (feature 1), located about 20 km from the mouth of the bay. Similar SAR signatures appear for other outflow plumes, e.g., the Rhine River [*Vogelzang et al.*, 1997; *Hessner et al.*, 2001]. In the absence of a strongly opposing wind, water in the outflow turns back toward the coast and flows southward as a narrow coastal current. These narrow currents have been observed in SAR imagery to extend more than 70 km along the coast [*Donato and Marmorino*, 2002]. The frontal signatures (feature 2) that are aligned approximately parallel to the coast correspond to the seaward edge of this coastal current. Because the water from the bay was warmer than the shelf water, both the plume and coastal current are further accentuated by generally higher radar backscatter through the effect of reduced atmospheric stability. Note, however, that a darker area of lower backscatter occurs along the coast southeast of Cape Henry (feature 3). The lower backscatter results from cooler shelf water that upwells near Cape Henry and subsequently flows back toward the mouth on flood tide [*Gallacher et al.*, 2000; *Marmorino et al.*, 2000]. The seaward edge of this wedge of denser water forms another convergent front that is also apparent in Figure 8.6. Although wind and stability effects are present, the frontal convergence is so strong that there is little doubt about the location of the current boundaries.

Additional SAR signatures appear within the mouth of the bay (features 4 and 5). These relatively bright or dark bands lie approximately over the edges of two channels that are used for navigation. Similar features occur along channels in smaller estuaries and rivers. The bright band corresponds to a region of converging currents. Converging currents can result from phase differences between the tidal current over the channel and the current over the adjacent shoals [e.g., *Valle-Levinson et al.*, 2000]. An alternative explanation is that a cross-channel circulation cell develops from vertical shear acting in the presence of the Earth's rotation. This circulation cell induces a surface convergence-divergence pair, which could account for the bright and dark bands in the imagery [*Handler et al.*, 2001]. Therefore, it is possible that SAR signatures of estuarine channels result from a combination of physical processes.

Added perspective and understanding of the underlying dynamics can be obtained from a sequence of radar images obtained during a tidal cycle. Such measurements for the Chesapeake Bay have been reported by *Sletten et al.* [1999], who used a real-aperture radar deployed on a Navy P-3 aircraft to observe fronts that formed within the mouth on flood tide and that translated seaward on the subsequent ebb tide. A new result is that bumps develop on the fronts and grow in amplitude during ebb tide. The sharp bend, or kink, appearing in the plume front in Figure 8.6 (feature 1) is likely an example of this. *Mied et al.* [2002] show how such growing frontal bumps can result from initial perturbations to the across-front velocity. A possible source for the initial perturbation is an abrupt change in bathymetry such as the change that occurs along shoal

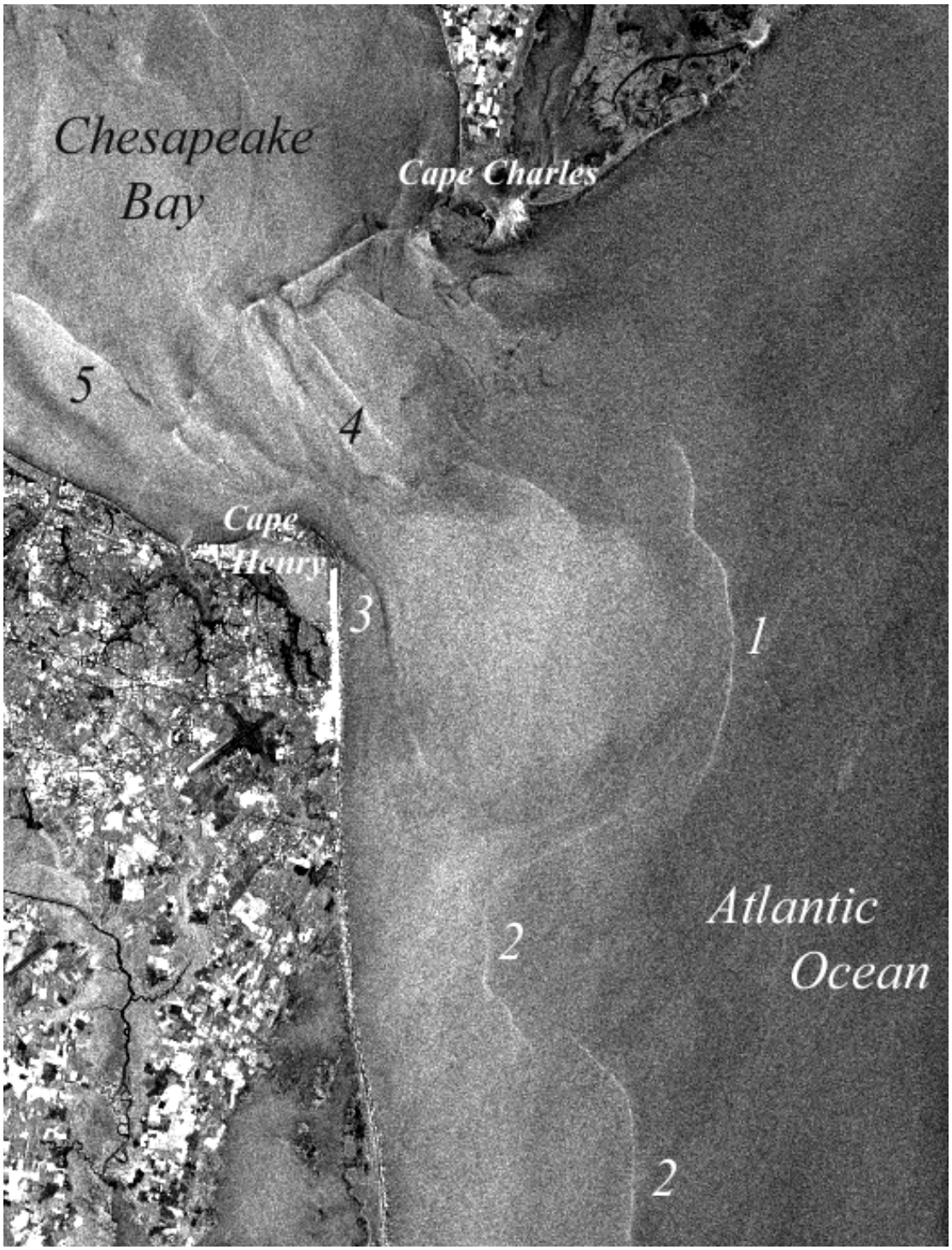

Figure 8.6. ERS-1 (C-band VV) SAR image of the lower Chesapeake Bay and adjoining continental shelf off the coast of Virginia (37 ^{o}N, 76 ^{o}W). Data were acquired during orbit 4257, at 0321 UTC on 9 May 1992. At that time, winds were about 6 m s^{-1} from the south (bottom of image) and the tidal current was about 1 hour into flood. Image resolution is about 100 m. The width of the bay mouth (Cape Henry to Cape Charles) is about 17 km. Figure modified from *Mied* [1997]. The numbers refer to features described in the test. Original image is ©ESA 1992 and was provided by Dr. Robert Beal (Johns Hopkins University Applied Physics Laboratory) from his US8-2c dataset.

regions in the bay mouth. Similar ongoing studies aim to better understand the details apparent in high-resolution radar imagery of estuarine areas.

8.5 Future Directions

The outlook for SAR oceanography continues to improve with the deployment of new spaceborne SAR systems such as ENVISAT (ESA, C-band, VV/HH), RADARSAT-2 (CSA, C-band, HH), and ALOS/PALSAR (NASDA, L-band, VV/HH). These systems offer wide swath imaging capabilities and will therefore significantly improve the temporal and spatial coverage needed to monitor the mesoscale current variability in coastal zones. It should be mentioned that ENVISAT includes an along-track scanning radiometer (AATSR) and an imaging spectrometer (MERIS) along with the imaging radar (ASAR), which offers the possibility of observing thermal fronts and water mass boundaries (under clear sky conditions) in addition to the surface roughness variations discussed in this chapter. Under conditions of partial cloud cover, SAR can also be used to connect sea surface temperature fronts masked by the clouds.

Quantitative estimation of currents or current gradients from SAR image intensity modulations remains a goal, but is contingent on further progress in modeling the effects of wave-current interactions. Such progress requires, among other things, a better parameterization of the source terms describing the growth of short gravity-capillary waves and the interaction of these waves with longer waves, including breaking waves. Another effect that needs to be better understood is the interdependence of wind stress, surface roughness, and atmospheric stability. In general, since the current information provided by SAR is area-extensive but indirect, this information is best used in the context of assimilation into oceanographic process models [*e.g. Johannessen et al*., 1993 and *Johannessen*, 2000].

A promising new technology for measuring ocean currents involves the use of two or more antennas separated in the along-track direction. The signals from these antennas are combined coherently to form a complex image (or interferogram), and the phase of the interferogram provides a direct measure of the radial velocity of the scatterers within each resolution cell. The scatterer velocity is related to the component of the surface current in the line of sight direction, but also includes contributions due to the phase velocity of the Bragg waves, so some interpretation of the data is required. The use of this technique for ocean current estimation has been demonstrated with airborne SAR systems [*Goldstein et al*., 1989; *Lyzenga and Malinas*, 1994; *Graber et al*., 1996]. The performance of the method depends on the ratio of the antenna spacing to the platform velocity, *i.e.* the time delay between looks. Thus, application of this method to spaceborne systems requires larger antenna separations than those used in airborne systems.

Although no satellite systems specifically designed for along-track interferometry are yet in operation, the Shuttle Radar Topography Mission (SRTM), which was flown on the Space Shuttle in February 2000, provided some preliminary information on the feasibility of such systems. The SRTM included two antennas separated by 60 m in the cross-track direction, intended for surface topographic measurements. For technical reasons, the antennas were not aligned exactly in the cross-track direction, and were in fact separated by 7 m in the along-track direction. Data from this mission has been analyzed by Romeiser et al. [2002] in order to estimate surface currents off the Dutch coast with some success, although better results would have been obtained with a larger along-track antenna spacing. As a result, Romeiser et al. [2003] have proposed similar experiments utilizing the split antenna planned for the German TerraSAR-X satellite to be launched in 2005. It should be noted that RADARSAT-2 will also have a split

antenna, and similar experiments could conceivably be carried out with this system. Of course, fore and aft looks would also be desirable in order to resolve both components of the surface current [*Frasier and Camps*, 2001].

Finally, the possibility of extracting surface current information using special processing of conventional spaceborne SAR data should be mentioned. This processing involves estimating the Doppler centroid of the SAR signals, which is done by Fourier transforming the complex image data in the azimuth direction. This technique was used with some success using aircraft SAR data but with very limited success using SEASAT SAR data [*Lyzenga et al.*, 1982; *Rufenach et al.*, 1983]. The limited success using SEASAT data may have been due to the (optical) processing method used and the frequency (L-band) of the SEASAT SAR. More promising results have been obtained recently by Chapron [2002] using a more sophisticated processing of C-band ENVISAT ASAR data. This processing includes a correction for Doppler centroid variations due to the antenna look direction, which is made possible by the precise orbital information available for ENVISAT. The spatial resolution is less than the nominal SAR resolution because a certain number of azimuth samples are required for the Doppler spectrum estimation and additional samples are required for averaging the estimates. The method has not yet been fully validated, but appears to warrant further development and evaluation.

8.6 References

Barnett, T. P., F. Kelly, and B. Holt, 1989: Estimation of the two dimensional ocean current shear field with a synthetic aperture radar. *J. Geophys. Res.*, **94**, 16 087–16 095.

Beal, R. C., T. W. Gerling, D. E. Irvine, F. M. Monaldo, and D. G. Tilley, 1986: Spectral variations of ocean wave directional spectra from the Seasat synthetic aperture radar. *J. Geophys. Res.*, **91**, 2433–2449.

——, V. N. Kudryavtsev, D. R. Thompson, S. A. Grodsky, D. G. Tilley, V. A. Dulov, and H. C. Graber, 1997: The influence of the marine atmospheric boundary layer on ERS-1 synthetic aperture radar imagery of the Gulf Stream. *J. Geophys. Res.*, **102**, 5799–5814.

Brown, R. A., 1990: Surface fluxes and remote sensing of air–sea interactions. *Current Theory*, G. L.Geernaert and W. J. Plant, Eds.,Vol. 1, Surface Waves and Fluxes, Kluwer Academic, 7–28.

Chapron, B., 2002: Ocean geophysical results from ASAR, *Envisat Validation Workshop*, 9-13 December 2002, ESRIN, Frascati, Italy.

Donato, T. F., and G. O. Marmorino, 2002: The surface morphology of a coastal gravity current. *Contin. Shelf Res*., **22**, 141–146.

Frasier, S.J., and A.J. Camps, 2001: Dual-beam interferometry for ocean surface current vector mapping, *IEEE Trans. Geosci. and Remote Sensing*, **39**, 401-414.

Fu, L.-L. and B. Holt, 1982: Seasat views oceans and sea ice with synthetic aperture radar. Jet Propulsion Laboratory JPL Pub. 81-120, Pasadena, CA, 200 pp.

——, and ——, 1983: Some examples of detection of oceanic mesoscale eddies by the Seasat synthetic aperture radar. *J. Geophys. Res.*, **88**, 1844–1852.

Gallacher, P. C., M. Schaferkotter, and P. Martin, 2000: Topographic and wind influences on the Chesapeake Bay outflow plume and the associated fronts. *Proc. 6th Int. Conf. on Estuarine and Coastal Modeling Meeting*, New Orleans, LA, ASCE, 443–451.

Goldstein, R. M., T. P. Barnett, and H. A. Zebker, 1989: Remote sensing of ocean currents. *Science*, **246**, 1282–1285.

Gower, J. F. R., 1994: Mapping coastal currents with SAR, using naturally-occurring surface slick patterns. *Proc. Second ERS-1 Symp.*, Hamburg, Germany, ESA, Publ. SP-361, 415–418.

Graber, H. C., D. R. Thompson, and R. E. Carande, 1996: Ocean surface features and currents measured with synthetic aperture radar interferometry and HF radar. *J. Geophys. Res*., **101**, 25 813–25 832.

Handler, R. A., R. P. Mied, T. E. Evans, and T. F. Donato, 2001: Convergence fronts in tidally forced rotating estuaries. *J. Geophys. Res*., **106**, 27 145–27 162.

Hayes, R. M., 1981: Detection of the Gulf Stream. *Spaceborne Synthetic Aperture Radar for Oceanography*, R. C. Beal, P. S. DeLeonibus, and I. Katz, Eds., Johns Hopkins Oceanogr. Studies, Vol. 7, 146–160.

Hessner, K., A. Rubino, P. Brandt, and W. Alpers, 2001: The Rhine outflow plume studied by the analysis of synthetic aperture radar data and numerical simulations. *J. Phys. Oceanogr*. **31**, 3030–3044.

Johannessen, J. A., 2000: Coastal observing systems: The role of synthetic aperture radar. *Johns Hopkins APL Tech. Dig.*, **21**, 41–48.

——, E. Svendsen, S. Sandven, O. M. Johannessen, and K. Lygre, 1989: Three dimensional structure of mesoscale eddies in the Norwegian coastal current. *J. Phys. Oceanogr.*, **19**, 3–19.

——, and Coauthors, 1993: Monitoring and modelling of the marine coastal environment. *Photogramm. Eng. Remote Sens.*, **59**, 351–361.

——, R. A. Shuchman, G. Digranes, D. Lyzenga, C. Wackerman, O. M. Johannessen, and P.W. Vachon, 1996: Coastal ocean fronts and eddies imaged with ERS-1 SAR. *J. Geophys. Res*., **101**, 6651–6668.

Lyzenga, D. R., 1991: Interaction of short surface and electromagnetic waves with ocean fronts. *J. Geophys. Res.*, **96**, 10 765–10 772.

——, 1998: Effects of intermediate-scale waves on radar signatures of ocean fronts and internal waves. *J. Geophys. Res.*, **103**, 18 759–18 768.

——, R.A. Shuchman, and C.L. Rufenach, 1982: Synthetic aperture radar measurements of ocean surface currents, *Geophys. Res. Letters*, **9**, 747-750.

——, and N. P. Malinas, 1994: Airborne radar measurements of coastal ocean currents and waves. *Proc. 2nd Thematic Conf. on Remote Sensing for Marine and Coastal Environments*, New Orleans, LA, ERIM, 379–388.

——, and C. C. Wackerman, 1997: Detection and classification of ocean eddies using ERS-1 and aircraft SAR images. *Proc. 3rd ERS Symp. on Space at the Service of our Environment*, Florence, Italy, ESA, Publ. SP-414, 1267–1271.

——, and G. O. Marmorino, 1998: Measurement of surface currents using sequential synthetic aperture radar images of slick patterns near the edge of the Gulf Stream. *J. Geophys. Res.*, **103**, 18 769–18 777.

Marmorino, G. O., and C. L. Trump, 2000: Gravity current structure of the Chesapeake Bay outflow plume. *J. Geophys. Res.*, **105**, 28 847–28 861.

——, T. F. Donato, M. A. Sletten, and C. L. Trump, 2000: Observations of an inshore front associated with the Chesapeake Bay outflow plume. *Contin. Shelf Res*., **20**, 665–684.

Mied, R. P., 1997: Use of remote imagery to obtain flow information in the littoral zone. *Rapid Environmental Assessment*, E. Pouliquen, A. D. Kirwan, and R. T. Pearson, Eds., SACLANTCEN Conference Proceedings Series CP-44, NATO SACLANT Undersea Research Centre, 127–130.

——, A. L. Cooper, G. J. Lindemann, and M. A. Sletten, 2002: Wave propagation along freely propagating surface gravity current fronts. *Dyn. Atmos. Oceans*, **36**, 59–81.

Munk, W., L. Armi, K. Fischer, and F. Zachariasen, 2000: Spirals on the sea. *Proc. Roy. Soc. London*, **A456**, 1217–1280.

Ochadlick, A. R., P. Cho, and J. Evans-Morgis, 1992: Synthetic aperture radar observations of currents colocated with slicks. *J. Geophys. Res.*, **97**, 5325–5330.

Romeiser, R., H. Breit, M. Eineder, and H. Runge, 2002: Demonstration of current measurements from space by along-track SAR interferometry with SRTM data, *Proc. 2002 International Geoscience and Remote Sensing Symposium (IGARSS 2002)*, **1**, 158-160, Inst. of Elec. and Electron. Eng., Piscataway, N.J., USA.

Romeiser, R., H. Breit, M. Eineder, H. Runge, P. Flament, K. de Jong, and J. Vogelzang, 2003: On the suitability of TerraSAR-X split antenna mode for current measurements by along-track interferometry, *Proc. 2003 International Geoscience and Remote Sensing Symposium (IGARSS 2003)*, 3 pp., Inst. of Elec. and Electron. Eng., Piscataway, N.J., USA.

Rufenach, C.L., R.A. Shuchman, and D.R. Lyzenga, 1983: Interpretation of Synthetic Aperture Radar Measurements of Ocean Currents, *J. Geophys. Res. 88*, 1867-1876.

Sletten, M. A., G. O. Marmorino, T. F. Donato, D. J. McLaughlin, and E. Twarog, 1999: An airborne, real-aperture radar study of the Chesapeake Bay outflow plume. *J. Geophys. Res.*, **104**, 1211–1222.

Sheres, D., 1982: Remote synoptic surface current measurements by gravity waves: A method and its test in a small body of water. *J. Phys. Oceanogr.*, **12**, 200–207.

Valle-Levinson, A., L. Chunyan, K. C. Wong, and K. M. M. Lwiza, 2000: Convergence of lateral flow along a coastal plain estuary. *J. Geophys. Res.*, **105**, 17 045–17 061.

Vogelzang, J., K. G. Ruddick, and J. B. Moens, 1997: On the signatures of river outflow fronts in radar imagery. *Int. J. Remote Sens.*, **18**, 3479–2505.

Wu, J., 1991: Effects of atmospheric stability on ocean ripples: A comparison between optical and microwave measurements. *J. Geophys. Res*., **96**, 7265–7269.